Computer Methods and Programs in Biomedicine 243 (2024) 107928

Contents lists available at ScienceDirect

Computer Methods and Programs in Biomedicine

journal homepage: www.elsevier.com/locate/cmpb

# Modelling coronary flow and myocardial perfusion by integrating a structured-tree coronary flow model and a hyperelastic left ventricle model

Yingjie Wang *, Xueqing Yin

*School of Mathematics and Statistics, University of Glasgow, Glasgow, United Kingdom*

ARTICLE INFO

*Keywords:*
Computational modelling
Structured-tree model
Vessel-myocardial interaction
Coronary flow
Myocardial blood flow

ABSTRACT

*Background and Objective:* There is an increasing demand to establish integrated computational models that facilitate the exploration of coronary circulation in physiological and pathological contexts, particularly concerning interactions between coronary flow dynamics and myocardial motion. The field of cardiology has also demonstrated a trend toward personalised medicine, where these integrated models can be instrumental in integrating patient-specific data to improve therapeutic outcomes. Notably, incorporating a structured-tree model into such integrated models is currently absent in the literature, which presents a promising prospect. Thus, the goal here is to develop a novel computational framework that combines a 1D structured-tree model of coronary flow in human coronary vasculature with a 3D left ventricle model utilising a hyperelastic constitutive law, enabling the physiologically accurate simulation of coronary flow dynamics.

*Methods:* We adopted detailed geometric information from previous studies of both coronary vasculature and left ventricle to construct the coronary flow model and the left ventricle model. The structured-tree model for coronary flow was expanded to encompass the effect of time-varying intramyocardial pressure on intramyocardial blood vessels. Simultaneously, the left ventricle model served as a robust foundation for the calculation of intramyocardial pressure and subsequent quantitative evaluation of myocardial perfusion. A one-way coupling framework between the two models was established to enable the evaluation and examination of coronary flow dynamics and myocardial perfusion.

*Results:* Our predicted coronary flow waveforms aligned well with published experimental data. Our model precisely captured the phasic pattern of coronary flow, including impeded or even reversed flow during systole. Moreover, our assessment of coronary flow, considering both globally and regionally averaged intramyocardial pressure, demonstrated that elevated intramyocardial pressure corresponds to increased impeding effects on coronary flow. Furthermore, myocardial blood flow simulated from our model was comparable with MRI perfusion data at rest, showcasing the capability of our model to predict myocardial perfusion.

*Conclusions:* The integrated model introduced in this study presents a novel approach to achieving physiologically accurate simulations of coronary flow and myocardial perfusion. It holds promise for its clinical applicability in diagnosing insufficient myocardial perfusion.

## 1. Introduction

The maintenance of adequate blood supply to myocardial tissues is crucial. Obstruction or constriction of major coronary vessels in the coronary vasculature causes inadequate myocardial perfusion which may lead to ischemia and bear the potential to progress to myocardial infarction and heart failure, thereby resulting in substantial morbidity and mortality [1]. Hence, it is important to understand coronary flow dynamics and accurately identify narrowed or obstructed major blood vessels in clinical settings. Imaging techniques, such as computed tomography (CT) and cardiovascular magnetic resonance (CMR) imaging, prove invaluable in visualizing coronary vasculature and detecting pathological anomalies [2–4]. Nevertheless, the intricate spatial and temporal variations within the coronary vasculature, along with the dynamic complexities of coronary flow, present challenges that hinder the investigation of myocardial perfusion. Thus, a comprehensive mathematical understanding of coronary flow is necessary [5–7]. Furthermore, the complex nature of coronary flow requires solid evidence

* Corresponding author.
*E-mail address:* y.wang.18@research.gla.ac.uk (Y. Wang).

https://doi.org/10.1016/j.cmpb.2023.107928
Received 26 September 2023; Received in revised form 2 November 2023; Accepted 13 November 2023
Available online 21 November 2023

for precise diagnosis and treatment planning of inadequate myocardial perfusion. As a result, an increasing necessity exists to establish computational models that incorporate assessments of coronary circulation and the interaction between blood flow and myocardial movement into the existing routine clinical workflow [8,9].

Moreover, the field of cardiology has shown an expanding pursuit towards personalised medicine, where computational models of the heart and coronary flow have the potential as valuable tools for integrating patient-specific diagnostic information [9,10]. These computational models can incorporate both physiological and mechanical principles of cardiovascular performance, by encompassing detailed geometric representations of the heart or coronary vasculature, thereby providing insightful perspectives. For precise prognostication of coronary flow and myocardial perfusion, an integrated model of both the heart and coronary flow is essential, considering the intricate interaction between cardiac movement and coronary perfusion. Consequently, considerable research efforts have been devoted to the development of the integrated models [11–16].

A one-dimensional (1D) computational model of blood flow, known as the structured-tree model, initially developed by Olufsen [17], holds the promising potential for integration within the integrated models. This model divides the arterial tree into two distinct components: large and small arteries. While the large arteries accurately replicate in vivo arterial geometry, small arteries are represented as binary asymmetric structured trees based on statistical relationships. Distinguishing itself from lumped parameter models [18,19], this 1D model effectively imitates wave propagation effects. Furthermore, it offers computational efficiency, making it valuable for clinical applications. Olufsen [17] employed this model to investigate blood flow waveforms in systemic arteries, later extended by Qureshi and Hill [20] to encompass hemodynamics of blood flow in pulmonary arteries. Duanmu et al. [21] utilised the structured-tree model for simulating blood flow in coronary arteries. However, their investigation excluded the venous aspect of the vascular system, which had previously been addressed by Vaughan [22] and Qureshi [23]. Additionally, they simplified the interaction between the myocardium and coronary flow by incorporating intramyocardial pressure (IMP) as a feedback mechanism for coronary flow.

IMP is the force exerted by myocardial tissues onto the external surfaces of intramyocardial blood vessels. In healthy individuals, heightened IMP during systole can impede coronary flow, even leading to retrograde flow [24,25]. The concept of the 'vascular waterfall' phenomenon, introduced by Downey and Kirk [26], elucidated for the first time how coronary flow is influenced by arterial pressure and IMP. Their experimental analysis of left coronary blood flow distribution across the canine heart wall during systole provided supporting evidence. Due to challenges in obtaining precise in vivo IMP measurements [27,28], researchers have recently turned to lumped-parameter models and three-dimensional (3D) heart models to estimate IMP [29,28,30,12,31]. For instance, Namani et al. [12] and Fan et al. [31] employed 3D idealised ellipsoidal left ventricle (LV) models to estimate IMP and coupled it into lumped parameter models of coronary flow. However, their work did not incorporate the orthotropic hyperelastic description of the myocardium, as proposed by Holzapfel and Ogden (HO model) [32]. The HO model has been widely utilised in computational heart models [33–35].

Motivated by the aforementioned limitations of existing computational models and the need to enhance our comprehension of myocardial perfusion, we have established a novel integrated computational model to explore coronary circulation. This model employs a one-way coupling framework of the 1D structured-tree model of coronary flow and a 3D LV model, enabling the evaluation of myocardial perfusion. Specifically, we calculate IMP from the LV model and incorporate it onto the external surfaces of intramyocardial blood vessels within the coronary flow model. Notably, in this study, the structured-tree model is extended to incorporate time-varying IMP into the governing equations of blood flow, reflecting its actual impact on coronary flow. Additionally, we employ the most up-to-date constitutive law, the HO model, to construct the LV model, which is an extension of our previous work [36]. To ensure the accuracy of our model, simulated coronary flow results are validated against experimental measurements of coronary flow waveforms and CMR perfusion data. Our novel integrated model demonstrates its capabilities in yielding physiological predictions of coronary flow and myocardial perfusion, as well as in clinical implications.

## 2. Methods

This study introduces an integrated model that combines a 1D structured-tree model for coronary flow dynamics with a 3D LV model to describe myocardial dynamics. In this section, we provide mathematical details of the 1D coronary flow model, the LV model, and the one-way coupling framework utilised to connect these two models.

### 2.1. One-dimensional coronary flow model

#### 2.1.1. A simplified coronary network

To analyse coronary flow within intricate coronary vasculature, as adopted in the structured-tree model [17,22,23], we divide the coronary vasculature into three distinct constituents: the epicardial coronary arteries, the epicardial coronary veins, and the remaining intramyocardial blood vessels. Following the terminology and methodology introduced by Olufsen [37], the large vessels including the epicardial coronary arteries and veins are collectively referred to as 'large vessels', while the smaller vessels within the myocardial wall are classified as 'small vessels'. Fig. 1 provides an illustration of a simplified human coronary vasculature network. Here, the large vessels are interconnected through binary trees consisting of compliant and tapering vessels, emulating the actual geometric characteristics of the human arterial tree. Conversely, the small vessels are modelled as binary asymmetric structured trees originating from the termini of the large arteries and eventually converging into the large veins. These small vessels are depicted as straight segments of compliant vessels and do not mimic the precise geometries of the vasculature. Instead, their representation is based on general statistical relationships.

Specifically, the large coronary arteries consist of left and right branches that originate from the aortic root. The left branch includes the left main coronary artery (LMCA), which bifurcates into the left anterior descending arteries (LAD, LAD1, LAD2, LAD3, and LAD4), the left circumflex arteries (LCX, LCX1, LCX2, and LCX3), and the marginal arteries (MARG1, MARG2, and MARG3). The right branch includes the proximal, middle, and distal right coronary arteries (RCA1, RCA2, and RCA3), which bifurcates into the conus branch, the right ventricular branch (RV branch), the acute marginal branch (AM branch), the posterior lateral artery (PLA), and the posterior descending artery (PDA). This simplified network is based on CT angiography of the coronary arteries by Duanmu et al. [21], alongside complementary information provided in [4,38,39]. Lengths, proximal radii, and distal radii of these vessels are summarised in Table 1.

The construction of the small vessels, namely the structured trees, are elaborated in [37,23]. In brief, the generation of these structured trees necessitates the use of radii and asymmetry relations at bifurcation points where a parent vessel splits into two daughter vessels, i.e.

$$r_{d_1} = \alpha r_p, \tag{1}$$

and

$$r_{d_2} = \beta r_p, \tag{2}$$

where the subscript $p$ refers to the parent vessel and the subscripts $d_1$ and $d_2$ represent the two daughter vessels, $\alpha = 0.9$ and $\beta = 0.6$ are two scaling factors that are assumed to be the same for all bifurcations [17]. These two scaling factors are determined through statistical relationships governing the branching pattern of the small vessels, which

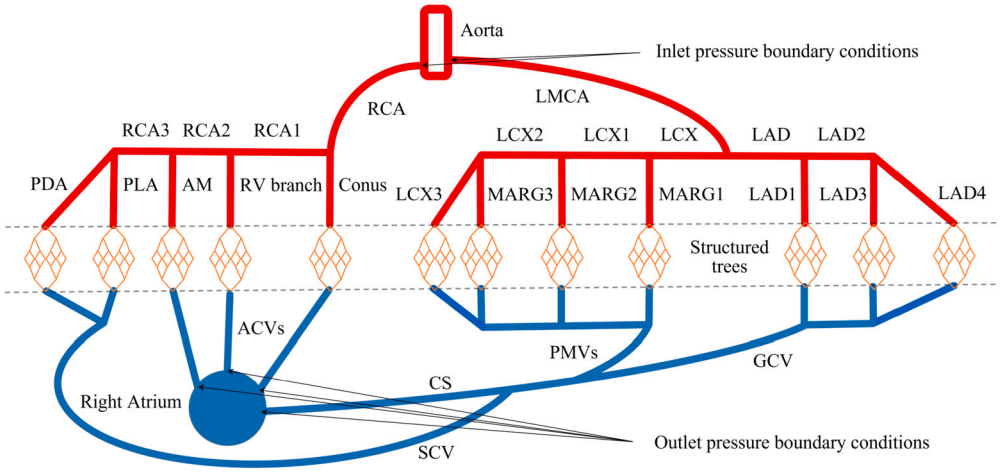


**Fig. 1.** A simplified network of human coronary vasculature. This network is divided into three distinct parts: the red vessels representing the epicardial arteries, the orange vessels (structured trees) representing intramyocardial vessels, and the blue vessels representing the epicardial veins. The dimensions of the epicardial arteries and veins are based on CT angiography by Duanmu et al. [21], supplemented by information from [4,38,39]. Notable epicardial coronary arteries and veins include LMCA (Left main coronary artery), LAD (Left anterior descending) arteries subdivided into LAD1, LAD2, LAD3, and LAD4, LCX (Left circumflex) arteries bifurcate into LCX1, LCX2, and LCX3, MARG (Marginal) arteries denoted as MARG1, MARG2, and MARG3, RCA (Right coronary artery) and its segments RCA1, RCA2 and RCA3, Conus, RV (Right ventricular) branch, AM (Acute marginal) branch, PLA (Posterolateral ventricular) artery, PDA (Posterior descending artery), CS (Coronary sinus), GCV (Great cardiac vein), PMVs (Left posterior and left marginal veins), SCV (Small cardiac vein), and ACVs (Anterior cardiac veins). It should be noted that while the generations of the epicardial arteries and veins are few, the intramyocardial vessels, which are represented by the structured trees, encompass approximately 50 generations, with each structured tree containing around 10 million vessels.

**Table 1**
Coronary artery dimensions in human vasculature, derived from experimental data by Duanmu et al. [21] and complementary literature sources [4,38,39].

| Branch | Length (cm) | Proximal radius (cm) | Distal radius (cm) | Branch | Length (cm) | Proximal radius (cm) | Distal radius (cm) |
|---|---|---|---|---|---|---|---|
| RCA1 | 3.7 | 0.151 | 0.150 | Conus | 3.3 | 0.112 | 0.108 |
| RCA2 | 3.6 | 0.150 | 0.149 | RV branch | 3.3 | 0.112 | 0.108 |
| RCA3 | 3.6 | 0.149 | 0.148 | AM | 3.3 | 0.112 | 0.108 |
| PLA | 4.2 | 0.128 | 0.125 | PDA | 3.7 | 0.108 | 0.105 |
| LMCA | 3.2 | 0.188 | 0.179 | LAD | 2.7 | 0.151 | 0.145 |
| LAD1 | 2.9 | 0.146 | 0.145 | LAD2 | 6.9 | 0.138 | 0.106 |
| LAD3 | 4.7 | 0.103 | 0.103 | LAD4 | 2.2 | 0.088 | 0.077 |
| LCX | 2.1 | 0.148 | 0.147 | LCX1 | 1.6 | 0.132 | 0.129 |
| LCX2 | 2.0 | 0.115 | 0.114 | LCX3 | 3.9 | 0.102 | 0.099 |
| MARG1 | 3.5 | 0.116 | 0.108 | MARG2 | 3.0 | 0.098 | 0.096 |
| MARG3 | 3.7 | 0.102 | 0.100 | | | | |

have been well documented in [37]. All the structured trees are ultimately terminated at a minimum radius of 0.0008 cm [40] before they access the capillary bed. For example, the generations of the structured tree connecting LAD1 to its venous counterpart, as shown in Fig. 1, are determined by the distal radius of LAD1 and the prescribed minimum termination radius. Additionally, at each branching point, the radii of the daughter vessels scale proportionally with parameters $\alpha$ and $\beta$. Owing to asymmetry, the arterial $\alpha$ branch of this structure tree comprises 56 generations, while the $\beta$ branch contains 10 generations. The collective count of vessels within this structured tree approximates 10 million. Considering the substantial number of vessels within the structured tree, we assume a homogeneous distribution of these vessels within the myocardium they perfuse to, ensuring the homogeneous distribution of blood to the myocardial tissue.

The reconstruction of the coronary venous system is referred to [39,41]. Fig. 1 illustrates the components of the venous system. It consists of the coronary sinus (CS), which receives blood from the great cardiac vein (GCV), left posterior and left marginal veins (PMVs), and small cardiac veins (SCV). These veins play a crucial role in draining a majority of blood from the LV wall and a portion of blood from the right ventricle wall. Conversely, the anterior cardiac veins (ACVs) primarily serve the purpose of draining the right ventricle wall and directly transporting the blood into the right atrium. The epicardial veins mirror the characteristics of the epicardial arteries, and therefore, their lengths are identical to those of their arterial counterparts. This decision is based on the observed parallel arrangement of epicardial arteries and veins [25]. Nevertheless, it is important to acknowledge that epicardial veins in general have larger radii in comparison to their arterial counterparts. Thus, we employ a vein-to-artery diameter ratio of 1.4, a value established in [42], to determine the radii of the veins based on the radii of their corresponding arteries. Furthermore, the CS deviates from this typical pattern. According to reports from [43–45], the CS exhibits an average length ranging from 3.5 to 6.3 cm and an average radius ranging from 0.353 to 0.590 cm. Therefore, for the CS, we assign an average length of 4.0 cm and an average radius of 0.478 cm.

### 2.1.2. Coronary flow dynamics

We modify the 1D structured-tree model developed by Qureshi and Hill [20] to simulate coronary flow dynamics. As described in the last section, the model simplifies the large vessels into elastic tapered tubes. We consider blood within these vessels to be homogeneous, viscous, and incompressible, characterised by a constant density $\rho = 1.055\,\mathrm{g/cm^3}$ and a viscosity $\mu = 0.490\,\mathrm{g/cm/s}$. Consequently, flow within the large vessels is a laminar flow. Coronary flow dynamics in these vessels are governed by the 1D reduced form of the Navier-Stokes equations:

$$\frac{\partial q}{\partial x} + \frac{\partial A}{\partial t} = 0, \tag{3}$$

and

$$\frac{\partial q}{\partial t}+\frac{\partial}{\partial x}\left(\frac{q^2}{A}\right)+\frac{A}{\rho}\frac{\partial p}{\partial x}=-\frac{2\pi\nu R}{\delta}\frac{q}{A}, \tag{4}$$

where $x$ is the axial coordinate, $t$ is the time, $q(x,t)$ is the volumetric flow rate, $A(x,t)$ is the cross-sectional area, $p(x,t)$ is the pressure, $\nu=0.4645\,\mathrm{cm}^2/\mathrm{s}$ is the kinematic viscosity, $R(x,t)$ is the vessel radius, and $\delta$ is the boundary layer thickness. The wall of the blood vessels is assumed to be isotropic and homogeneous, and a tube law is prescribed as follows

$$\phi(x,t)=p(x,t)-p_0=\frac{4}{3}\frac{Eh}{r_0}\left(\sqrt{\frac{A}{A_0}}-1\right), \tag{5}$$

where $\phi(x,t)$ is the transmural pressure, $p_0$ is a trivial external pressure exerted by the pericardium on the large vessels, $E$ is Young's modulus, $h$ is the vessel wall thickness, and $r_0$ and $A_0$ are the initial stress-free radius and cross-sectional area, respectively. The inverse of $4Eh/3r_0$ is the distensibility of the vessel, reflecting the elastic characteristics of the vessel wall and its responsiveness to transmural pressure. Qureshi and Hill [20] applied a constant distensibility assumption to large pulmonary arteries and veins, setting it at $0.0038\ \mathrm{mmHg}^{-1}$. In this study, we adopt a constant distensibility value of $0.0011\ \mathrm{mmHg}^{-1}$ for the large coronary arteries and veins. This choice is based on measurements of coronary vessel distensibility derived from porcine subjects [46].

In contrast, for the small vessels within structured trees, the nonlinear effects of coronary flow are neglected, and a linearised model can be analytically solved according to [17,20]. In circulatory systems, the pressure and flow rate are periodic due to the contraction and relaxation of the heart. Therefore, we assume periodicity in coronary flows with a period of $T=0.8\,\mathrm{s}$ and an angular frequency $\omega=2\pi/T$. By expanding the flow rate and transmural pressure into the Fourier series, their Fourier coefficients can be calculated by

$$Q_k(x)=\frac{1}{q_c}\left(a_k\cos(k\omega x/c)+b_k\sin(k\omega x/c)\right), \tag{6}$$

$$\Phi_k(x)=\frac{i}{\rho g l C c}(-a_k\sin(k\omega x/c)+b_k\cos(k\omega x/c)), \tag{7}$$

where $k$ is the $k$th Fourier component, $q_c$ is the characteristic flow rate, $a_k, b_k$ are constants dependent on the specific pressures at the inlet and outlet of a small vessel, $c$ is the wave propagation velocity, $g$ is the acceleration of gravity, $l$ is the characteristic length, and $C=0.0055$ $\mathrm{mmHg}^{-1}$ is the constant distensibility of all the small vessels. Eq. (6) and Eq. (7) are utilised to obtain a great admittance of a whole structured tree. The great admittance serves as a linking condition to relate the frequency-domain transmural pressure $\Phi_k(L)$ and flow rate $Q_k(L)$ at the outlet of a large terminal artery (such as LAD1) with frequency-domain transmural pressure $\Phi_k(0)$ and flow rate $Q_k(0)$ at the inlet of a large terminal vein (such as GCV), i.e.

$$\begin{pmatrix}Q_k(L)\\ Q_k(0)\end{pmatrix}=\mathbf{Y}_k\begin{pmatrix}\Phi_k(L)\\ \Phi_k(0)\end{pmatrix}, \tag{8}$$

where $\mathbf{Y}_k$ is the great admittance matrix. Using the convolution integral, Eq. (8) in the frequency domain can be transformed into two equations in the real-time domain:

$$q(L,t)=\frac{1}{T}\int_{-T/2}^{T/2}(\phi(L,t-\tau)y_{11}(\tau)+\phi(0,t-\tau)y_{12}(\tau))d\tau, \tag{9}$$

and

$$q(0,t)=\frac{1}{T}\int_{-T/2}^{T/2}(\phi(L,t-\tau)y_{21}(\tau)+\phi(0,t-\tau)y_{22}(\tau))d\tau, \tag{10}$$

where $y_{11}(t), y_{12}(t), y_{21}(t), y_{22}(t)$ are the inverse Fourier transforms of the four components of the great admittance $\mathbf{Y}_k$. Eq. (9) and Eq. (10) are the so-called structured-tree matching boundary condition that connects the flow from the large arteries to the large veins. It is important to highlight that this matching condition serves the purpose of establishing a correlation between transmural pressure and flow rate. This differs from the correlation between blood pressure and flow rate utilised in previous research by Qureshi and Hill [20] for pulmonary circulation, where the time-varying IMP was not taken into account.

Lastly, the coronary flow within the simplified network in Fig. 1 is determined by solving equations (3), (4), and (5). The two-step Lax-Wendroff method [47] is adopted to obtain numerical solutions. This is accomplished by incorporating appropriate inlet and outlet pressure boundary conditions, time-varying IMP, and the structured-tree matching condition. Additionally, it is assumed that no energy dissipation occurs at each bifurcation of the large vessels within the simplified network. Thus, the flow rate and pressure of a parent vessel and its two daughter vessels at each bifurcation point satisfy the following two bifurcation conditions:

$$q_p(L,t)=q_{d_1}(0,t)+q_{d_2}(0,t), \tag{11}$$

and

$$p_p(L,t)=p_{d_1}(0,t)=p_{d_2}(0,t), \tag{12}$$

where $L$ indicates the outlet of the parent vessel and 0 indicates the inlet of the two daughter vessels.

### 2.2. Three-dimensional left ventricle model

To simulate physiologically accurate motion and deformation of LV, we have developed a 3D finite element (FE) LV model. The schematic representation of our LV model is shown in Fig. 2. This model consists of a patient-specific LV mesh, a commonly used myofibre architecture, and a lumped parameter model to represent systemic circulation. The 3D LV geometry is reconstructed from short-axis slices from the LV base to the LV apex and three long-axis slices of the LV of a healthy volunteer through CMR. Details on the reconstruction process are referred to [48]. The resulting LV geometry is discretised into a tetrahedral mesh using ICEM (ANSYS, Inc. PA USA), comprising 133,042 elements and 26,010 nodes, as shown in Fig. 2 (a). This mesh serves as the foundation for computational analysis using the FE method. Additionally, a rule-based myofibre structure [49,50] is generated based on the tetrahedral mesh. Fig. 2 (b) illustrates the orientation of the myofibres, which vary linearly from $-60°$ at the epicardium to $60°$ at the endocardium. This myofibre architecture follows a widely adopted convention in the literature [51, 36].

As shown in Fig. 2 (c), a simplified open-loop lumped parameter model representing the systemic circulation is coupled with the LV cavity. This coupling enables the lumped parameter model to provide physiologically accurate LV cavity pressure, which plays a crucial role in determining the movement of the LV. To enclose the LV cavity, we employ two-dimensional triangular surface elements, previously introduced in studies by Baillargeon et al. [52] and Sack et al. [34]. The relationships of pressures ($P_{\mathrm{LV}}$, $P_{\mathrm{Ao}}$, $P_{\mathrm{SA}}$) and volumes ($Q_{\mathrm{LV}}$, $Q_{\mathrm{Ao}}$, $Q_{\mathrm{SA}}$) of the three cavities, as shown in Fig. 2 (c), can be expressed as follows:

$$\frac{\mathrm{d}Q_e}{\mathrm{d}t}=C_e\frac{\mathrm{d}P_e}{\mathrm{d}t}, \tag{13}$$

and

$$Q_{e\to e+1}=\frac{\Delta P_{e\to e+1}}{R_{e\to e+1}}, \tag{14}$$

where $e=\{\mathrm{LV},\mathrm{Ao},\mathrm{SA}\}$, $C_e$ is the compliance of each cavity, $Q_{e\to e+1}$ is the flow rate between any two neighboring cavities, $\Delta P_{e\to e+1}$ is the pressure difference, and $R_{e\to e+1}$ is the resistance. A constant pressure of 8 mmHg is imposed at the outlet boundary, representing the pressure of the systemic veins (SV). According to [36], the compliance and resistance values are $C_{\mathrm{Ao}}=2.5\,\mathrm{mL/mmHg}$, $C_{\mathrm{SA}}=1.25\,\mathrm{mL/mmHg}$,

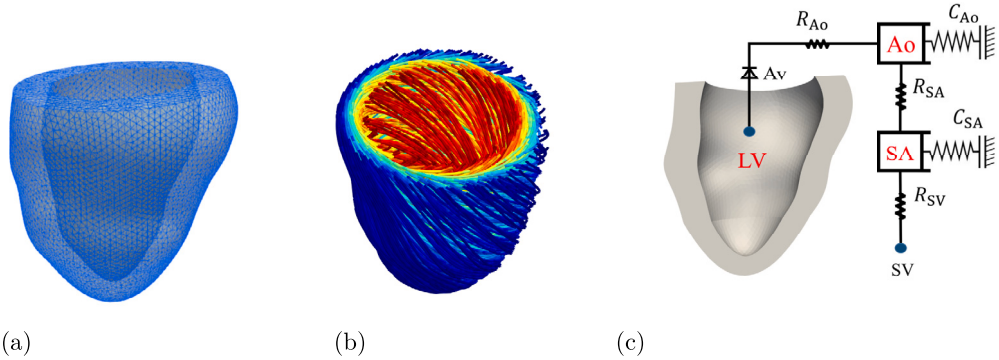


**Fig. 2.** A schematic illustration of our human left ventricle (LV) model. The tetrahedral mesh (a) consists of 133,042 linear elements and 26,010 nodes. A rule-based myofibre architecture of the myocardium (b) shows the myofibre angle ranging from −60° at the epicardium to 60° at the endocardium. In (c), the LV cavity is interconnected with a lumped parameter model to represent systemic circulation. The components include the aortic valve (Av), aorta (Ao), systemic arteries (SA), and systemic veins (SV). The aortic valve is symbolised by the Diode symbol, indicating unidirectional flow. Resistances $R_{Ao}$, $R_{SA}$, and $R_{SV}$ are associated with the aortic valve, systemic arteries, and a trivial resistance allowing drainage of the flow in the systemic circulation, respectively. Compliances $C_{Ao}$ and $C_{SA}$ represent the aortic and systemic arterial compliances.

$R_{Ao} = 2.0\,\text{MPa}\cdot\text{s/m}^3$, and $R_{SA} = 120.0\,\text{MPa}\cdot\text{s/m}^3$. Additionally, $R_{SV} = 0.8\,\text{MPa}\cdot\text{s/m}^3$ is a minor resistance that allows the flow drainage within this open-loop system.

### 2.2.1. Passive constitutive law

The passive material property of the myocardium can be characterised by the orthotropic hyperelastic model proposed by Holzapfel and Ogden [32]. Their model takes into account the layered myofibre architecture and introduces three mutually orthogonal principal directions, namely the unit myofibre direction $\mathbf{f}_0$, the unit sheet direction $\mathbf{s}_0$, and the unit sheet-normal direction $\mathbf{n}_0$ in a reference configuration. The strain energy function is

$$\psi = \frac{a}{2b}\exp[b(I_1-3)] + \frac{a_\text{f}}{2b_\text{f}}\left\{\exp[b_\text{f}(\max(I_{4\text{f}},1)-1)^2]-1\right\} + \frac{a_\text{s}}{2b_\text{s}}\left\{\exp[b_\text{s}(\max(I_{4\text{s}},1)-1)^2]-1\right\} + \frac{a_\text{fs}}{2b_\text{fs}}\left\{\exp[b_\text{fs}I_{8\text{fs}}^2]-1\right\}, \tag{15}$$

where the eight material constants according to [36] are $a = 0.1731$ kPa, $b = 5.1207$, $a_\text{f} = 1.9344$ kPa, $b_\text{f} = 0.2199$, $a_\text{s} = 0.2143$ kPa, $b_\text{s} = 0.0005$, $a_\text{fs} = 0.2665$ kPa, $b_\text{fs} = 2.5505$, $I_1$ is the trace of the right Cauchy-Green deformation tensor $\mathbf{C}$, and $I_{4\text{f}}$, $I_{4\text{s}}$, and $I_{8\text{fs}}$ are the invariants related to the myofibre and sheet directions, i.e.

$$I_{4\text{f}} = \mathbf{f}_0\cdot(\mathbf{C}\mathbf{f}_0), \quad I_{4\text{s}} = \mathbf{s}_0\cdot(\mathbf{C}\mathbf{s}_0), \quad I_{8\text{fs}} = \mathbf{f}_0\cdot(\mathbf{C}\mathbf{s}_0), \tag{16}$$

where the invariants $I_{4\text{f}}$ and $I_{4\text{s}}$ represent the squared stretches along the myofibre direction and the sheet direction, respectively. The utilisation of the max() function ensures that myofibres exclusively experience tensile stress, preventing any compressive load. To facilitate the FE computational algorithm, the strain energy function in Eq. (15) is further decomposed into a volumetric part and a deviatoric part.

### 2.2.2. Active tension model

The active tension ($T_\text{a}$) generated by the myocardium during systole is determined through a well-established time-varying elastance model [53]

$$T_\text{a}(t,l) = \frac{T_\text{max}}{2}\,\frac{\text{Ca}_0^2}{\text{Ca}_0^2 + \text{ECa}_{50}^2(l)}\,(1-\cos(\omega(t,l))), \tag{17}$$

where $T_\text{max} = 110$ kPa is the maximum isometric active tension, $\text{Ca}_0 = 4.35\,\mu$M is the peak intra-cellular calcium. The length-dependent calcium sensitivity is given by

$$\text{ECa}_{50}(l) = \frac{\text{Ca}_{0\text{max}}}{\sqrt{e^{B(l-l_0)}-1}}, \tag{18}$$

where $B = 4.750\,\mu\text{m}^{-1}$ and $\text{Ca}_{0\text{max}} = 4.35\,\mu$M, $l_0 = 1.58\,\mu$m is the minimum sarcomere length to produce active stress, and $l$ is the deformed sarcomere length, i.e.

$$l = l_r\sqrt{2E_\text{ff}+1}, \tag{19}$$

where $l_r = 1.85\,\mu$m is the stress-free sarcomere length, and $E_\text{ff}$ is the Lagrange strain in the myofibre direction. The time function after the onset of contraction in Eq. (17) is

$$\omega(t,l) = \begin{cases} \pi\,\frac{t}{t_0} & \text{for} \quad 0 \leqslant t \leqslant t_0, \\ \pi\,\frac{t-t_0+t_r(l)}{t_r} & \text{for} \quad t_0 < t \leqslant t_0+t_r, \\ 0 & \text{for} \quad t > t_0+t_r, \end{cases} \tag{20}$$

where $t_0 = 0.18$ s is the time to peak tension, and $t_r$ is the duration of relaxation

$$t_r(l) = ml + b, \tag{21}$$

where $m = 1.0489\,\text{s/}\mu\text{m}$ and $b = -1.7$ s are constants to determine the shape of the linear relaxation duration and sarcomere length relaxation. This active tension is incorporated into the Cauchy stress using the active stress approach [52,34,36]. Finally, the dynamics of the LV are governed by

$$\begin{cases} \nabla\cdot\boldsymbol{\sigma} = 0, & \text{within the LV wall,} \\ \boldsymbol{\sigma}\cdot\mathbf{n} = -P\mathbf{n}, & \text{on the LV endocardial surface,} \\ \boldsymbol{\sigma}\cdot\mathbf{n} = 0, & \text{on the LV epicardial surface,} \\ u_\theta = 0 \quad \text{and} \quad u_z = 0, & \text{on the LV basal surface,} \end{cases} \tag{22}$$

where $\boldsymbol{\sigma}$ is the Cauchy stress, $\mathbf{n}$ is the unit vector normal to the LV endocardial or epicardial surface, $P$ denotes the LV cavity pressure, and $u_\theta$ and $u_z$ are the displacements along the $\theta$-axis and the $z$-axis, respectively, within a global cylindrical coordinate system. This coordinate system centres around the origin of the LV basal plane, with its $z$-axis corresponding to the long-axis direction of the LV. Constraints are applied to the LV basal surface to restrict movement in both the long-axis and circumferential directions. This constraint approach, ensuring realistic expansion and contraction of the LV basal plane, has been adopted by Thekkethil et al. [54].

## 2.3. One-way coupling framework

The one-way coupling framework is established through the following steps: Firstly, a standalone simulation of the 3D LV model is conducted to acquire essential data including aortic pressure and IMP.

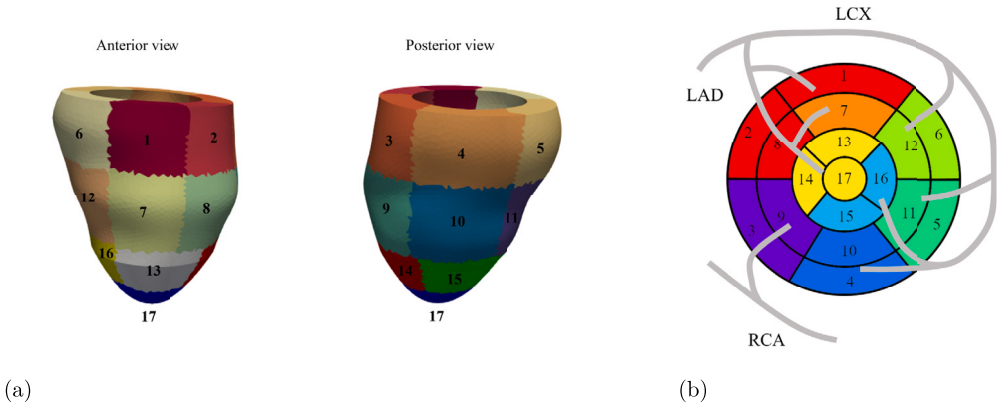


**Fig. 3.** Anterior and posterior perspectives (a) of 17 segments of a left ventricle (LV) wall according to the recommendation of American Heart Association [57]. These segments are systematically numbered from 1 to 17 to facilitate their identification and categorization. A polar perspective (b) displays the LV segments and their association with the terminal branches of the three main coronary arteries, namely the left anterior descending artery (LAD), left circumflex artery (LCX), and right coronary artery (RCA). The allocation is visually differentiated through colour coding, signifying the specific assignment of each terminal branch to its respective LV region.

It should be noted that the IMP is calculated as the hydrostatic pressure based on the Cauchy stress [55], expressed as

$$\mathrm{IMP} = \frac{1}{3}\mathrm{trace}(\boldsymbol{\sigma}). \tag{23}$$

Subsequently, both the simulated aortic pressure and IMP are utilised in the 1D coronary flow model. To drive coronary flow within the simplified network, the simulated aortic pressure serves as the inlet pressure boundary condition, applied at the inlets of the LMCA and RCA as shown in Fig. 1. Meanwhile, the simulated IMP is integrated into Eq. (9) and Eq. (10) to dynamically regulate coronary flow by altering the admittance of the structured trees. In addition, for the coronary flow model, the outlet pressure boundary condition is assumed to be 3.0 mmHg. This value corresponds to the mean right atrial pressure, typically ranging from zero to 5.0 mmHg [56]. These outlet pressure boundary conditions are applied at the outlets of the ACVs and CS as shown in Fig. 1. Lastly, myocardial perfusion is determined by associating coronary arteries with corresponding LV wall segments.

The assignment between epicardial coronary arteries and LV wall segments assumes critical importance in the diagnosis and management of cardiovascular diseases. The assignment aids the evaluation of motion abnormalities of myocardial segments, perfusion defects, and myocardial viability during imaging examinations such as echocardiography and CMR. In accordance with the guidelines established by the American Heart Association (AHA) [57], a comprehensive evaluation of myocardial perfusion and function necessitates the utilisation of a 17-segment model, as visually represented in Fig. 3 (a). Thus, we propose the following allocation that assigns the epicardial coronary arteries to the 17 LV segments, by leveraging the spatial information concerning coronary arteries provided by Cerci et al. [58]. All the terminal branches of the epicardial coronary arteries in the simplified network (Fig. 1) are correlated with the 17 LV segments, as summarised in Table 2. Specifically, LAD1 supplies blood to LV segments 1, 2, and 8; LAD4 supplies blood to segment 7; LAD3 supplies blood to segments 13, 14, and 17; MARG1 perfuses segments 6 and 12; MARG2 perfuses segments 5 and 11; MARG3 perfuses segments 15 and 16; LCX3 perfuses segments 4 and 10; and PDA is responsible for nourishing segments 3 and 9.

A graphical representation illustrating the assignment of the terminal branches to the 17 LV segments is further provided in Fig. 3 (b). In line with this assignment, the LV wall is subdivided into distinct regions as distinguished by different colours, each receiving blood supply from specific terminal arteries: LAD1, LAD4, LAD3, MARG1, MARG2, MARG3, LCX3, and PDA. For example, the LAD1-perfused region, consisting of segments 1, 2, and 8, receives myocardial perfusion from

**Table 2**
Coronary artery assignment to left ventricle (LV) segments recommended by the American Heart Association (AHA) guidelines [57]. This assignment is based on spatial information of the coronary arteries in [58].

| Coronary artery | Spatial information [58] | AHA LV segment [57] |
|---|---|---|
| LAD1 | First diagonal branch | 1, 2, 8 |
| LAD4 | Second diagonal branch | 7 |
| LAD3 | Distal LAD | 13, 14, 17 |
| MARG1 | First obtuse marginal branch | 6, 12 |
| MARG2 | Second obtuse marginal branch | 5, 11 |
| MARG3 | Third obtuse marginal branch | 15, 16 |
| LCX3 | Left posterior descending branch | 4, 10 |
| PDA | Posterior descending artery | 3, 9 |

LAD1. Through the utilisation of the one-way coupling framework, the computation of regionally-averaged IMP and corresponding myocardial perfusions becomes feasible.

Myocardial perfusion refers to the dynamic process of blood circulation that furnishes the myocardium with vital oxygen and nutrients. To quantify myocardial perfusion by the indicator 'myocardial blood flow (MBF)', we propose the following equation

$$\mathrm{MBF} = \frac{\int_0^T q\,\mathrm{d}t}{T\,m_{\mathrm{myo}}}, \tag{24}$$

where $q$ is the coronary flow rate, measured at the endpoint of a terminal artery, i.e. the truncation point where the artery enters the myocardium, $T$ represents the duration of a single cardiac cycle, and $m_{\mathrm{myo}}$ is the myocardial mass within the region perfused by the terminal artery. This approach enables the quantification of myocardial perfusion, holding the potential to improve clinical decision-making in various cardiovascular diseases.

### 2.4. Implementation

The implementation of the coronary flow model involves the integration of pre-existing C++ and Fortran programs, initially developed by Olufsen [37] and subsequently extended by Qureshi [23] to investigate systemic and pulmonary circulations, respectively. Building upon their foundational work, we have expanded their model and programs in this study to explore the dynamics of coronary circulation, wherein time-varying IMP plays an important role in modulating coronary flow. In parallel, the LV model is implemented in ABAQUS 2018 (Dassault Systèmes, Johnston, RI, USA) [59], with the constitutive law being incorporated through the VUMAT user subroutine. To implement the lumped-parameter system in the LV model, the fluid cavity and fluid

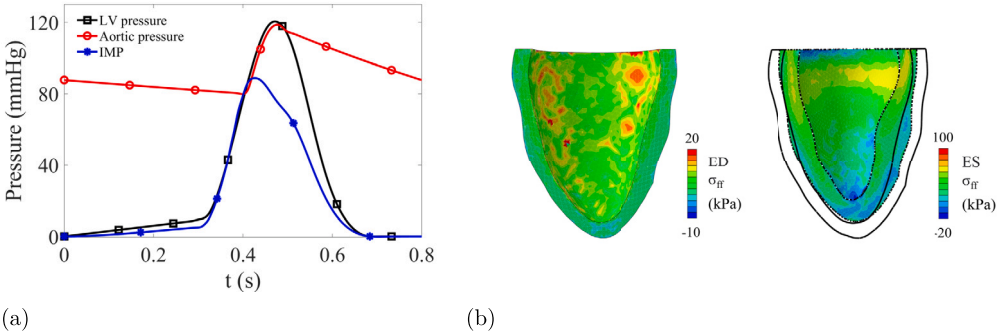


**Fig. 4.** Simulated left ventricle (LV) pressure, aortic pressure, and globally-averaged intramyocardial pressure (IMP) from the LV model throughout the third cardiac cycle (a). Distributions of the myofibre stress $\sigma_{ff}$ at the end of diastole (ED) and the end of systole (ES) are shown in (b). The solid black outlines representing LV geometry at ED are used for reference.

**Table 3**
Comparison between average myofibre stress (unit: kPa) from our left ventricle model simulation and published data. ED: end of diastole. ES: end of systole.

| | Genet et al. [65] | Sack et al. [67] | Sack et al. [34] | Fan et al. [68] | Our simulation |
|---|---|---|---|---|---|
| ED | $2.21 \pm 0.58$ | $1.47 \pm 20.72$ | $2.1 \pm 4.2$ | 2.53 | 3.26±16.42 |
| ES | $16.54 \pm 4.73$ | $14.45 \pm 106.72$ | $18.6 \pm 14.9$ | 36.08 | 27.32±26.33 |

exchange modulus of ABAQUS are employed. Analogous approaches for implementing heart models have been utilised in previous studies [52,34,36].

The duration of a single cardiac cycle in this study is defined as 0.8 seconds, corresponding to a heart rate of 75 beats per minute. Utilising a Linux workstation equipped with 8 cores of 2.3 GHz CPU (Intel(R) Xeon(R) CPU E5-2699 v3) and 128 GB memory, the simulation of five consecutive cardiac cycles of the coronary flow model takes approximately 15 minutes. Conversely, the simulation of five consecutive cardiac cycles of the LV model requires around 10 hours. Notably, both models achieve stability after the third cycle. Consequently, the subsequent results section exclusively presents outcomes within the third cycle.

## 3. Results

Simulated LV pressure, aortic pressure, and globally-averaged IMP throughout a complete cardiac cycle derived from the LV model are shown in Fig. 4 (a). The LV pressure linearly increases from zero to 8.0 mmHg within zero to 0.3 s. The systolic phase, spanning 0.3 to 0.5 s, is marked by a rapid LV pressure ascent, peaking at 119.6 mmHg. Simultaneously, the simulated aortic pressure ranges between 79.8 mmHg and 118.7 mmHg, closely resembling the physiological range in healthy individuals (80.0 mmHg to 120.0 mmHg) [60,61]. The mismatch between the LV pressure and aortic pressure during ejection, while aortic valve opening, remains within 10.0 mmHg [62]. The globally-averaged IMP within the LV wall reaches a maximum of 88.5 mmHg around 0.42 s. Following aortic valve closure, both the LV pressure and the IMP decrease to zero. It is noteworthy that the aortic pressure undergoes near-linear reduction during diastole due to the utilisation of a simplified lumped parameter system for systemic circulation representation. Furthermore, the end-diastolic volume of the LV is 109.5 ml, with an end-systolic volume of 45.9 ml, yielding an LV ejection fraction of 58%. This ejection fraction agrees with the typical range for healthy individuals, spanning from 50% to 65% [63,64].

Distributions of myofibre stress $\sigma_{ff}$ at the end of diastole (ED) and end of systole (ES) are shown in Fig. 4 (b). These distributions exhibit heterogeneity. At ED, some regions on the LV endocardial surface display high stresses. Across the myocardial wall, myofibre stress is higher in the subendocardial layers compared to the subepicardial layers. The LV geometry at ED is outlined in solid black to reveal LV contraction and long-axis shortening. The transmural distribution of myofibre stress at ES is non-monotonic. In the basal and middle regions, $\sigma_{ff}$ is mostly highly positive in the middle layers of the LV wall but has lower positive values at the epicardial and endocardial surfaces. Conversely, in the apical regions, $\sigma_{ff}$ exhibits negative values in the middle layers, along with both the epicardial and endocardial surfaces. These observations are comparable with stress distributions reported in [65,34,66]. For instance, Genet et al. [65] found that their simulated myofibre stress at ED was higher near the subendocardial wall than near the subepicardial wall. At ES, the myofibre stress was higher in the middle layer of the myocardium, particularly in the basal regions. Furthermore, Sack et al. [34] presented their heterogeneous myofibre stress distribution in a long-axis cut plane of the LV. In their findings, at ED, the maximum myofibre stress was predominantly localised in the subendocardial and basal regions. As for ES, high myofibre stress was observed in the middle and endocardial layers of the LV wall, particularly near the basal and middle regions, while myofibre stress was negative near the apical regions.

Average myofibre stresses across the entire LV wall at ES and ED are summarised in Table 3, alongside average stresses from prior research studies [65,67,34,68]. These studies report average myofibre stress at ED ranging from 1.47 kPa to 2.53 kPa, and at ES spanning from 14.45 kPa to 36.08 kPa. Specifically, compared to the results in [68], our simulated average myofibre stress at ED is 3.26 kPa, reflecting a 28.9% increase over their reported value. Conversely, our average myofibre stress at ES is 27.32 kPa, signifying a 24.3% decrease relative to their reported value. It is important to acknowledge that variations in average myofibre stress across different studies are to be expected due to differences in geometries, material models, and boundary conditions.

Simulated regionally-averaged IMPs from the LV model are illustrated in Fig. 5. These IMP curves exhibit a gradual rise across various LV regions during zero to 0.3 s, followed by a rapid ascent towards their respective peaks, and subsequently declining to zero around 0.7 s. The IMPs remain at zero until 0.8 s. The peak values of the regionally-averaged IMPs range from 36.4 mmHg in the LAD3-perfused region to 114.9 mmHg in the LCX3-perfused region. The IMP of the PLA-perfused region is included to illustrate the assumed IMP within the right ventricle wall, equating to one-third of the globally-averaged IMP across the entire LV wall, considering the absence of the right ventricle in our model. The globally-averaged IMP in the right ventricle wall peaks at 29.5 mmHg. Moreover, these peaks emerge at different time points. For

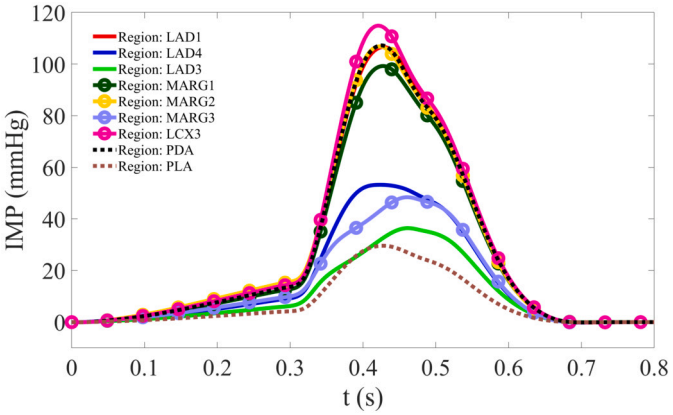


**Fig. 5.** Simulated regionally-averaged intramyocardial pressure (IMP) in the left ventricle wall. IMPs vary across distinct regions nourished by the terminal arteries: LAD1, LAD4, LAD3, MARG1, MARG2, MARG3, LCX3, and PDA. Additionally, PLA is included to illustrate the assumed IMP in the right ventricle wall.

instance, the IMP of the LAD3-perfused region reaches its maximum value 0.05 seconds after the peak IMP of the LAD4-perfused region.

The aforementioned aortic pressure and regionally-averaged IMPs serve as boundary conditions for the coronary flow model. Simulated flow rates in the LAD and LCX arteries, along with their comparison to experimental data from studies conducted by Duanmu et al. [21], Mynard et al. [69], and Fan et al. [30], are shown in Fig. 6. Overall, the simulated LCX and LAD flow rates exhibit comparable values with experimental data and follow the same trend. In Fig. 6 (a), our simulated LCX flow rate ranges from -0.55 $cm^3/s$ to 1.03 $cm^3/s$, with a mean value of 0.64 $cm^3/s$. In comparison, the experimental LCX flow rate obtained from domestic swine by Fan et al. [30] varies from -0.39 $cm^3/s$ to 1.35 $cm^3/s$, with a mean value of 0.43 $cm^3/s$. Furthermore, the experimental LCX flow rate acquired from newborn lamb by Mynard et al. [69] ranges from -0.71 $cm^3/s$ to 1.90 $cm^3/s$, with a mean value of 0.91 $cm^3/s$. Additionally, the experimental LCX flow rate obtained from a male patient by Duanmu et al. [21] varies between 0.82 $cm^3/s$ and 1.81 $cm^3/s$, with a mean value of 1.49 $cm^3/s$. It can be observed that the experimental LCX flow rate reported by Duanmu et al. [21] is comparatively higher than the other two experimental studies. As shown in Fig. 6 (b), our simulated LAD flow rate ranges from -0.23 $cm^3/s$ to 0.79 $cm^3/s$. In comparison, the experimental LAD flow rate obtained by Duanmu et al. [21] from a male patient ranges from 0.56 $cm^3/s$ to 1.96 $cm^3/s$, while the experimental LAD flow obtained by Fan et al. [30] from swine ranges from -0.47 $cm^3/s$ to 1.63 $cm^3/s$.

The impeding of the coronary flow in the LCX and LAD arteries during systole, as indicated by the two vertical lines in Fig. 6, aligns with previous finding [25]. Moreover, it can be observed that both the simulated LCX and LAD flow rates during systole exhibit three local extrema ($P_1$, $P_2$, and $P_3$). Following 0.3 s, the systolic phase commences, accompanied by a substantial increase in the IMPs that cause compression of intramyocardial blood vessels, leading to minimal flow rates ($P_1$) for both LCX and LAD arteries. This corresponds to the peak values of the regionally-averaged IMPs at about 0.41 s, as shown in Fig. 5. Subsequently between approximately 0.41 s and 0.46 s, as the IMPs begin to decline but the aortic pressure remains increasing, the flow rates in the LCX and LAD arteries increase. Around 0.46 s, coinciding with the occurrence of the maximum aortic pressure as shown in Fig. 4 (a), the LCX and LAD flow rates reach their respective local peaks ($P_2$). Following $P_2$, the LCX and LAD flow rates gradually decrease which can be attributable to the reduction in both the aortic pressure and IMPs. At approximately 0.5 s, local minimum points ($P_3$) are observed. It should be mentioned that due to the simplified nature of our reconstructed coronary network compared to in vivo networks, the experimental data

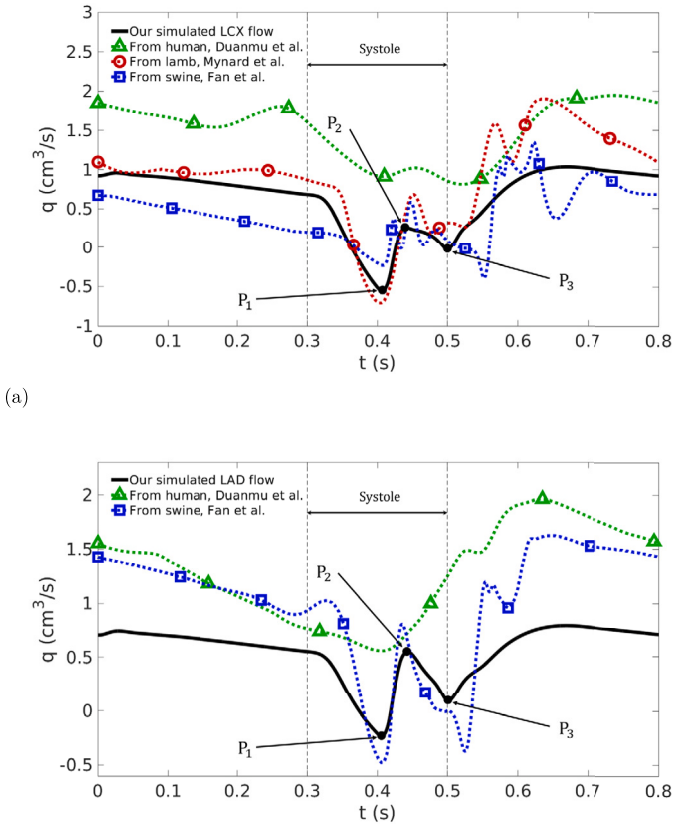


**Fig. 6.** Simulated coronary flow in LCX (a) and LAD (b) arteries. This is achieved by the one-way coupling framework where aortic pressure and regionally-averaged intramyocardial pressure are derived from our left ventricle model. The simulated outcomes are compared with experimental data from [21,69,30]. Notably, three local extrema ($P_1$, $P_2$, and $P_3$) are identified during systole within the time interval specified by the vertical dashed lines.

exhibit greater variability than our simulated results, showing more fluctuations in coronary flow.

The application of regionally-averaged IMP has led to coronary flow results that align with physiological characteristics. For a more comprehensive understanding of the influence of IMP variations on coronary flow, we conduct a comparative analysis of coronary flow using globally-averaged IMP. In Appendix A, a comparison of simulated flow rates in LCX and LAD using globally-averaged IMP and AHA regionally-averaged IMP reveals only minor differences in flow rates between the two cases. However, substantial disparities emerge when considering the flow rates of the terminal vessels, as shown in Fig. 7. Specifically, Fig. 7 (a) illustrates that employing globally-averaged IMP leads to nearly overlapping flow rates in the three terminal vessels of the LCX branch: MARG2, MARG3, and LCX3. Conversely, employing regionally-averaged IMP generates distinct flow rates for the three vessels. In the MARG2-perfused region, MARG3-perfused region, and LCX3-perfused region, the maximum regionally-averaged IMP values are 107.1 mmHg, 48.4 mmHg, and 114.9 mmHg, respectively. Therefore, the MARG3-perfused region experiences the lowest IMP, causing the least impedance to MARG3's flow rate during systole. In contrast, the LCX3-perfused region displays the highest regionally-averaged IMP, leading to the greatest impedance to LCX3's flow rate during systole. Moreover, it can be observed that the effect of IMP on coronary flow is more pronounced during systole than diastole. Additionally, as shown in Fig. 7 (b), the influence of globally-averaged and regionally-averaged IMP on the flow rates of the three terminal vessels in the LAD branches (LAD1, LAD4, and LAD3) closely mirrors the observed trends in the LCX branches. In brief, flow rates in these vessels exhibit greater variation

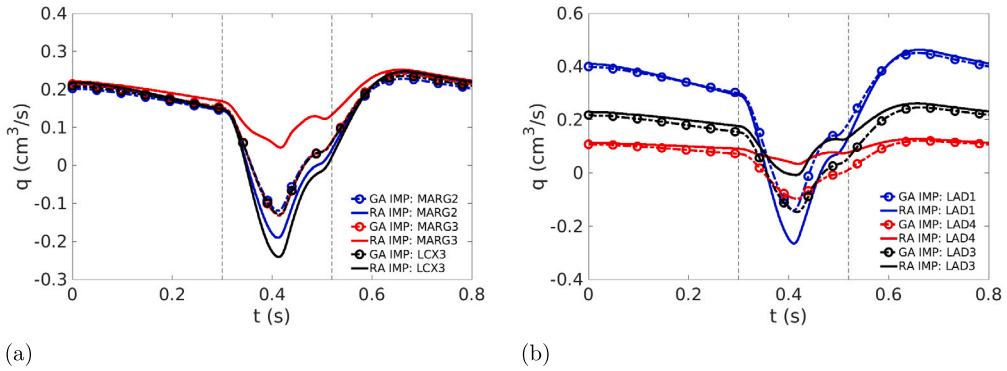


**Fig. 7.** Comparing simulated flow rates in select terminal arteries of LCX branches (a) and LAD branches (b). Flow rates in LCX branches (MARG2, MARG3, LCX3) and LAD branches (LAD1, LAD4, LAD3) are compared using globally-averaged and regionally-averaged intramyocardial pressure (IMP), respectively. Abbreviations 'GA IMP' and 'RA IMP' denote globally and regionally averaged IMP.

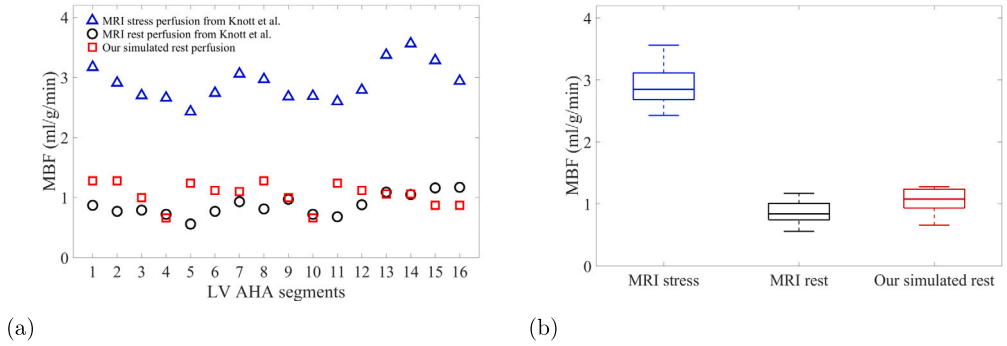


**Fig. 8.** Simulated myocardial perfusion (a) in the first 16 AHA segments [57] of the left ventricle wall assessed by the myocardial blood flow (MBF). Comparison with MRI rest and stress MBF from Knott et al. [70] is presented. Box plots (b) illustrate distributions of the three datasets.

during systole than diastole, and increased flow impedance is caused by higher IMP. For instance, the flow rate in the LAD1 experiences the most significant impediment, corresponding to the highest IMP in the LAD1-perfused region.

Utilising our one-way coupling framework and employing regionally-averaged IMP, we present MBF values for the first 16 AHA segments in Fig. 8 (a), alongside a comparison with MRI data of a healthy subject from Knott et al. [70]. MBF in the 17th AHA segment is excluded due to insufficient experimental data for comparison. It can be found that our simulated MBF values are comparable with the MRI rest MBF measurements. Notably, the MRI stress MBF exhibits significantly higher values than the rest MBF. Furthermore, Fig. 8 (b) presents box plots illustrating the distribution of the three datasets. Our one-way coupling model predicts a range of rest MBF spanning from 0.66 ml/g/min to 1.28 ml/g/min, with a median value of 1.08 ml/g/min and a mean of 1.05 ml/g/min. In comparison, the MRI rest MBF ranges from 0.56 ml/g/min to 1.17 ml/g/min, with a median of 0.84 ml/g/min and a mean of 0.87 ml/g/min. Our simulated mean rest MBF surpasses the MRI rest MBF by 20.7%.

## 4. Discussion

We have developed a novel integrated model through a one-way coupling framework, incorporating the 1D structured-tree coronary flow model with the 3D LV model to simulate physiologically realistic coronary flow and myocardial perfusion. The simplified coronary network, constructed based on experimental data from Duanmu et al. [21], facilitated coronary flow simulation along the entire course of coronary vasculature, spanning from the aortic root to the right atrium. Moreover, we extended the structured-tree model to incorporate time-varying IMP, thereby addressing scenarios where blood flow could be impeded due to IMP-induced compression of the coronary vasculature. Our simulated coronary flow results reflected characteristic waveforms and values within the normal range, closely aligning with experimental data reported in the literature. This accurate simulation of coronary flow was accomplished by employing the one-way coupling framework, which allowed for the exploration of vessel-myocardial interaction and enabled a deeper investigation of myocardial perfusion. The LV model, utilising the patient-specific geometry and the HO constitutive law, facilitated accurate IMP calculation. Simulated LV pressure and aortic pressure from this LV model fell within physiological ranges, and we further compared average myofibre stress with other simulation studies. In this section, we discuss the modelling assumptions and findings while also providing limitations and directions for future research.

### 4.1. Simplified coronary network

In our study, a simplified coronary network was devised based on realistic human coronary artery anatomy. In the realm of computational modelling for coronary flow, the incorporation of a detailed computational network of coronary vasculature is pivotal for accurate flow and pressure predictions. Research on coronary vasculature anatomy has a well-established history [71–73]. Notably, Kassab et al. [72] advanced this field by providing a comprehensive dataset of coronary vasculature in healthy young farm pigs, along with a diameter-defined Strahler model for subsequent hemodynamic analyses. Smith et al. [74] adopted the provided connectivity, vessel radius, and length distributions to construct a geometric coronary model encompassing the first six generations of the largest coronary arterial vessels. More comprehensive efforts in coronary arterial network reconstruction are available in the literature [75–77]. It is important to note that the reconstructed coronary networks in these studies are notably complex, largely due to the extensive presence of intramyocardial blood vessels. This complexity poses a significant challenge for coronary vasculature reconstruction,

which in turn increases computational costs associated with coronary flow simulations [72,74].

In contrast, the structured-tree model represents the extensive intramyocardial blood vessels as binary structured trees, reducing the need for precise morphological and topological information about these vessels. This approach significantly simplifies coronary vasculature reconstruction, leading to reduced computational costs, which is particularly crucial for clinical applications. We also constructed a venous system, as shown in Fig. 1. Coronary veins exhibit greater morphological variability compared to arteries and geometric data on the veins are limited [41,39,78]. Therefore, our simplified coronary network only included the CS, GCV, PMVs, SCV, and ACVs based on existing descriptions of the venous system in [41,39]. These veins collectively constitute the greater cardiac venous system, responsible for collecting about 70% of deoxygenated blood within the coronary vasculature. It should be noted that blood in the ACVs directly drains into the right atrium.

### 4.2. Intramyocardial pressure

Our model effectively captured the essential phasic pattern of coronary flow, as shown in Fig. 6, by introducing the one-way coupling between IMP and coronary flow. This novel approach included the time-varying IMP in the equations of the structured-tree model for the first time. As explained in Section 2.1.1, the structured-tree model divides coronary blood vessels into two main components: the epicardial blood vessels, encompassing both epicardial arteries and veins situated on the heart's surface, and the intramyocardial blood vessels, including arterioles, capillaries, and venules positioned within the heart wall. The fundamental interaction between the myocardium and coronary flow predominantly takes place through the intramyocardial blood vessels. Specifically, as outlined by the tube law in Eq. (5), transmural pressure, denoting the difference between blood pressure and IMP, regulates the cross-sectional areas of the intramyocardial blood vessels. IMP fluctuates during each cardiac cycle, thereby leading to corresponding changes in the cross-sectional areas of the intramyocardial blood vessels. In particular, during systole, IMP significantly rises, causing constriction in the intramyocardial blood vessels and consequent reduction in the volume of the vascular bed. This constriction propels blood into both arterial and venous sides of the coronary vasculature. As a result, the blood pressure gradient from upstream to downstream is not the sole determinant of coronary blood flow; rather, IMP assumes a crucial role in determining coronary flow dynamics. Elevation in IMP will counteract the driving force of coronary flow, highlighting a distinct feature that sets coronary circulation apart from systemic and pulmonary circulations. Within the coronary circulation, a majority of arterial flow occurs during diastole, while during systole, the arterial flow may slow down or even undergo reversal as a consequence of the elevated IMP [24,5,25].

In this study, we have adopted the hydrostatic pressure derived from the Cauchy stress tensor to calculate IMP [55]. Multiple approaches for IMP calculation have been documented in the literature [29,28,12,30]. For instance, Namani et al. [12] employed the following approach:

$$\mathrm{IMP} = \frac{1}{2}(\sigma_{\mathrm{ss}} + \sigma_{\mathrm{nn}}) + \alpha(1 - \lambda_{\mathrm{f}}), \tag{25}$$

where $\sigma_{\mathrm{ss}}$ and $\sigma_{\mathrm{nn}}$ are the stress in the sheet direction and sheet-normal direction, respectively, $\alpha$ is a constant, and $\lambda_{\mathrm{f}}$ is the myofibre stretch. Fan et al. [30,31], on the other hand, calculated IMP by the Lagrange multiplier. Despite variations in these approaches, their simulated peak IMPs generally ranged from 70.0 mmHg to 140.0 mmHg. Our model estimated the peak value of globally-averaged IMP across the entire LV wall to be 88.5 mmHg, which agrees with the literature.

It is noteworthy that invasive experiments utilising needle or pipette measurements have been conducted to quantify IMP in various animal hearts [27]. Nevertheless, despite advancements in measurement techniques, the accurate spatial and temporal distribution of IMP within the heart wall remains elusive due to challenges posed by cardiac motion, potential tissue microstructure distortion caused by the pipette tip, and the heterogeneous nature of pressure within different microcompartments of the myocardium. Consequently, while recent modelling studies have proposed various approaches to calculate IMP [29,28,12,30], most of these models primarily validate their flow waveforms against experimental data, rather than the IMP itself. Therefore, there continues to be a scarcity of reliable experimental IMP data within this research area.

### 4.3. Myocardial blood flow

By conducting a comparative assessment of flow rates in select terminal vessels under the influence of globally-averaged IMP versus regionally-averaged IMP, as shown in Fig. 7, our study demonstrated the significant role of IMP magnitude in governing coronary flow. Higher IMP values correspond to increased coronary flow impediment. Thus, the impact of IMP on coronary flow is more prominent during systole compared to diastole, because IMP during diastole is relatively low. Furthermore, the disparities observed in the flow rates of the terminal vessels between the two cases lead to variations in myocardial perfusion. Employing regionally-averaged IMP yielded a mean MBF of 1.05 ml/g/min in the LV wall. In contrast, the utilisation of globally-averaged IMP resulted in a mean MBF of 1.02 ml/g/min, indicating comparability between the two cases. However, the adoption of globally-averaged IMP led to more dispersed MBF outcomes, as evidenced by a standard deviation of 0.28. Conversely, employing regionally-averaged IMP yielded a lower standard deviation of 0.20.

Measured MBF values in the literature [79,80,70], providing insights into normal MBF ranges among healthy individuals at rest and stress, can be found in Table B.4 in Appendix B. Specifically, Brown et al. [79] conducted a study involving 42 healthy subjects (23 females, median age 23 years) and found mean MBF at rest to be 0.64±0.15 ml/g/min, increasing to 2.55±0.57 ml/g/min under stress. Kotecha et al. [80] reported mean MBF at rest as 0.78±0.18 ml/g/min in their study involving 15 control subjects. They observed stress MBF at 3.17±0.65 ml/g/min, and in regions with obstructive coronary artery disease, a mean stress MBF of 1.47 ml/g/min and myocardial perfusion reserve of 1.75. Furthermore, Knott et al. [70] recruited 24 healthy volunteers (12 females, mean age 37.3 years) and found mean MBF at rest to be 0.86 ml/g/min, increasing to 3.07 ml/g/min under stress.

In comparison to the mean MBF values at rest in these studies, our model predicted higher rest MBF. This discrepancy can be attributed to the mismatch between the coronary network and the LV geometry employed in our study. Our coronary network originated from CT image data of a male patient [21], whereas, to ensure physiologically accurate LV dynamics, we employed a female LV geometry from a prior study [48] due to the unavailability of corresponding LV geometry. It has been documented in a study [81] that the mean LV mass is 155.1 g for males and 103.0 g for females. Consequently, our utilisation of a lighter female LV geometry contributes to the calculated higher rest MBF compared to the reported values.

### 4.4. Limitations and future perspectives

There are several limitations associated with this study. Firstly, the mismatch between the coronary network and the LV geometry resulted in elevated rest MBF in comparison to published data. However, the methodology established in this study can be readily adapted to accommodate varied heart geometries and coronary vasculature. Consequently, this limitation can be addressed through the integration of both coronary network and heart geometry derived from the same patient. With the continuous advancements in imaging techniques and the accessibility of comprehensive datasets, our model exhibited the potential to enhance the precision of MBF predictions. Additionally, it is important to acknowledge that the assignment of epicardial coronary arteries to the 17 AHA segments of the LV wall in this study was based on

general spatial information of coronary arteries in [58]. However, the morphology of the coronary vasculature is complex and varies significantly among individuals. These variations encompass differences in vessel caliber, alternative branch morphologies, and dominance patterns within the coronary vasculature. Thus, a patient-specific approach is necessary for accurately assigning coronary arteries to LV segments. Moreover, the assumptions regarding the constant elastic properties of vessel walls in our model necessitate refinement through the incorporation of more sophisticated nonlinear models to accurately emulate realistic physiological conditions [82,7]. We have so far maintained the assumption of constant distensibility in both epicardial arteries and veins, a notion supported by studies such as [46], which indicate constant distensibility in porcine coronary arteries within a pressure range of 60-140 mmHg. Nevertheless, it is essential to recognise two critical considerations. First, distensibility exhibits a correlation with vessel diameter, tending to decrease as vessel diameter increases. Second, epicardial veins possess thinner walls and greater distensibility compared to arteries. However, establishing comprehensive quantitative relationships between distensibility, vessel geometry, and mechanical properties, especially within the context of human vasculature, remains a challenging and ongoing endeavour. Collectively, these aspects highlight the need for further endeavours to translate clinical and experimental information into computational models [9].

Secondly, a sensitivity analysis of all parameters and an uncertainty quantification analysis were not conducted in this study. The primary objective of our investigation was to develop the computational models and establish the coupling framework. Future studies can undertake these analyses to enhance the robustness of our model and its predictive capabilities across a wide spectrum of physiological and pathological conditions. For example, performing a comprehensive parameter variation analysis that encompasses the radii of both epicardial and intramyocardial vessels, along with adjustments in heart rate, can facilitate the simulation of coronary flow under stress conditions. It is important to note that in our current model, we utilised data on epicardial artery radii acquired during maximum hyperemia [21]. While these epicardial vessels are fully dilated, they are not sufficient to account for the overall reduction of resistance within the entire coronary vasculature, as the majority of resistance originates from the millions of vessels within the structured trees. Hence, by incorporating further dilation of vessels with diameters smaller than 100 μm [83] and increasing the heart rate and cardiac output in the LV model, we can simulate coronary flow during exercise. Moreover, our model offers the potential for exploring pathological states [84–86]. For instance, it can be employed to calculate coronary fractional flow reserve by simulating the occlusion of specific epicardial coronary arteries within the simplified network.

Thirdly, this study has only achieved a one-way coupling between the coronary flow model and the LV model, primarily focusing on exploring the effect of IMP on coronary flow and myocardial perfusion. To progress towards bidirectional coupling, the subsequent phase involves investigating the effect of myocardial perfusion on cardiac functions, such as myocardial work and contractility [29,87,16]. Overcoming this limitation entails linking cardiac functions with myocardial perfusion to achieve a balance between myocardial oxygen supply and demand [88]. A recent study by Fan et al. [30] introduced a relationship between myocardial contractility and coronary flow, distinguishing between ischemic and non-ischemic regimes. Within the ischemic regime, myocardial contractility demonstrates linear variation with total coronary flow, while in the non-ischemic regime, coronary flow remains constant, namely coronary flow having no impact on contractility. The contractility in their model was determined by maximal chamber elastance, which in our model can be determined by the scaling factor, $T_{\max}$, in the active contraction model. Therefore, integrating such a relationship into our model will facilitate the achievement of a bidirectional coupling between the coronary flow model and the LV model. In fact, as there is no effect of coronary flow on myocardial contractility for non-ischemic regimes, our model can be regarded as a bidirectional coupling framework. Nevertheless, this changes when coronary flow does influence myocardial contractility.

## 5. Conclusion

This study presented a novel one-way coupling framework that integrates a 1D structured-tree coronary flow model with a 3D hyperelastic LV model, yielding physiologically accurate coronary flow and myocardial perfusion. To the best of our knowledge, this is the first instance of such a study based on the structured-tree model of coronary simulation. We introduced a simplified coronary network for human vasculature and extended the structured-tree model to coronary circulation by incorporating time-varying IMP on the outer surfaces of intramyocardial blood vessels. The 3D LV model provided a computational way to estimate IMP which plays an important role in the vessel-myocardial interaction. Furthermore, we established an assignment of the epicardial coronary arteries to the 17 AHA LV segments. Simulated coronary flow waveforms were validated against experimental data. It was observed that the simulated coronary flow slows down or even reverses during systole. Three local extrema of the flow rates during systole were also identified. Finally, the one-way coupling framework enabled myocardial perfusion calculation through MBF. The simulated MBF values were comparable with MRI results. Overall, our model demonstrated promising capabilities to provide accurate predictions of coronary flow and myocardial perfusion, with further exploration expected to enhance our comprehension of coronary circulation and mechanisms underlying cardiovascular diseases resulting from inadequate myocardial perfusion, via computational modelling.

## Declaration of competing interest

The authors declare that they have no conflict of interest.

## Acknowledgements

Y. Wang acknowledges funding from the Chinese Scholarship Council and the fee waiver from the University of Glasgow. The authors thank Dr. Hao Gao, Dr. Zheng Duanmu, Prof. Xiaoyu Luo, and Prof. Nick Hill for sharing the patient information and guidance in the modelling work.

## Appendix A. Comparison of simulated flow rates in LCX and LAD using globally-averaged IMP and regionally-averaged IMP

The averaged IMP is calculated based on the Cauchy stress of all elements in different regions. This involves using the finite element method to determine Cauchy stress values at each element. The volumetric average of IMP in different regions is calculated as:

$$\overline{\mathrm{IMP}} = \frac{\sum_{i=1}^{n} (\mathrm{IMP}_i)\, V_i}{\sum_{i=1}^{n} V_i}, \tag{A.1}$$

where $\mathrm{IMP}_i$ is the IMP at the centroid of the $i^{th}$ element, $V_i$ is the volume of the $i^{th}$ element, and $n$ is the total number of the elements occupied by different regions. In our study, we define two distinct volumetric-averaged IMP metrics. One is the globally-averaged IMP, which averages IMP across the entire LV wall. Consequently, the globally-averaged IMP is consistent at all positions within the LV wall. The other metric is the regionally-averaged IMP. In contrast, the regionally-averaged IMP is determined by averaging IMP within the 17 different AHA regions. As a result, this metric varies across different regions.

To compare the effect of globally-averaged IMP and regionally-averaged IMP on simulated coronary flow, Fig. A.9 illustrates flow rates of LCX and LAD for both scenarios. Overall, differences in LCX and LAD flow rates between the two cases are minor. In LCX flow rates, utilising regionally-averaged IMP yields higher values during diastole but

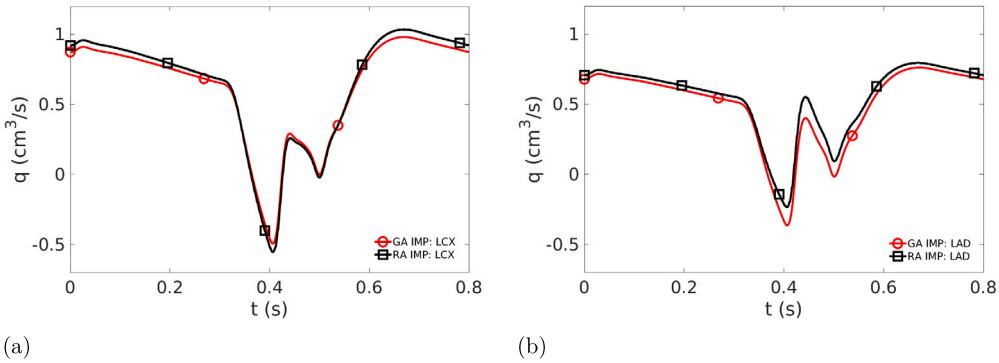


**Fig. A.9.** Comparison of simulated flow rates in LCX (a) and LAD (b) using globally-averaged and regionally-averaged intramyocardial pressure (IMP), respectively. Abbreviations 'GA IMP' and 'RA IMP' denote globally and regionally averaged IMP.

**Table B.4**
Measured myocardial blood flow (MBF) at rest and stress in the literature [79,80,70] for healthy individuals.

| Reference | Number of healthy individuals | MBF (ml/g/min) at rest | MBF (ml/g/min) at stress |
|---|---|---|---|
| Brown et al. [79] | 42 | 0.64±0.15 | 2.55±0.57 |
| Kotecha et al. [80] | 15 | 0.78±0.18 | 3.17±0.65 |
| Knott et al. [70] | 24 | 0.86 | 3.07 |

slightly lower values during systole in comparison to globally-averaged IMP. Conversely, in both systole and diastole, LAD flow rates using regionally-averaged IMP are greater than those using globally-averaged IMP. These observations indicate that employing globally-averaged IMP can yield satisfactory coronary flow simulations in proximal coronary arteries, including the initial branches of LCX and LAD.

## Appendix B. Measured MBF values in the literature

The MBF values at rest and stress conditions of healthy individuals reported in the literature [79,80,70] are summarised in Table B.4.

## References

[1] A.N. Nowbar, M. Gitto, J.P. Howard, D.P. Francis, R. Al-Lamee, Mortality from ischemic heart disease: analysis of data from the world health organization and coronary artery disease risk factors from ncd risk factor collaboration, Circ. Cardiovasc. Qual. Outcomes 12 (6) (2019) e005375.
[2] A. Sato, H. Ohigashi, T. Nozato, H. Hikita, M. Tamura, S. Miyazaki, Y. Takahashi, T. Kuwahara, A. Takahashi, M. Hiroe, et al., Coronary artery spatial distribution, morphology, and composition of nonculprit coronary plaques by 64-slice computed tomographic angiography in patients with acute myocardial infarction, Am. J. Cardiol. 105 (7) (2010) 930–935.
[3] M. Loukas, A. Sharma, C. Blaak, E. Sorenson, A. Mian, The clinical anatomy of the coronary arteries, J. Cardiovasc. Transl. Res. 6 (2013) 197–207.
[4] K. Hirai, T. Kido, T. Kido, R. Ogawa, Y. Tanabe, M. Nakamura, N. Kawaguchi, A. Kurata, K. Watanabe, O. Yamaguchi, et al., Feasibility of contrast-enhanced coronary artery magnetic resonance angiography using compressed sensing, J. Cardiovasc. Magn. Reson. 22 (1) (2020) 1–10.
[5] N. Westerhof, C. Boer, R.R. Lamberts, P. Sipkema, Cross-talk between cardiac muscle and coronary vasculature, Physiol. Rev. 86 (4) (2006) 1263–1308.
[6] J. Lee, N.P. Smith, The multi-scale modelling of coronary blood flow, Ann. Biomed. Eng. 40 (11) (2012) 2399–2413.
[7] G. Kassab, Coronary Circulation, Springer, 2019.
[8] J. Lee, D. Nordsletten, A. Cookson, S. Rivolo, N. Smith, In silico coronary wave intensity analysis: application of an integrated one-dimensional and poromechanical model of cardiac perfusion, Biomech. Model. Mechanobiol. 15 (6) (2016) 1535–1555.
[9] S.A. Niederer, J. Lumens, N.A. Trayanova, Computational models in cardiology, Nat. Rev. Cardiol. 16 (2) (2019) 100–111.
[10] M. Peirlinck, F.S. Costabal, J. Yao, J. Guccione, S. Tripathy, Y. Wang, D. Ozturk, P. Segars, T. Morrison, S. Levine, et al., Precision medicine in human heart modeling, Biomech. Model. Mechanobiol. (2021) 1–29.
[11] S.M. Shavik, L. Zhong, X. Zhao, L.C. Lee, In-silico assessment of the effects of right ventricular assist device on pulmonary arterial hypertension using an image based biventricular modeling framework, Mech. Res. Commun. 97 (2019) 101–111.
[12] R. Namani, L.C. Lee, Y. Lanir, B. Kaimovitz, S.M. Shavik, G.S. Kassab, Effects of myocardial function and systemic circulation on regional coronary perfusion, J. Appl. Physiol. 128 (5) (2020) 1106–1122.
[13] L. Papamanolis, H.J. Kim, C. Jaquet, M. Sinclair, M. Schaap, I. Danad, P. van Diemen, P. Knaapen, L. Najman, H. Talbot, et al., Myocardial perfusion simulation for coronary artery disease: a coupled patient-specific multiscale model, Ann. Biomed. Eng. 49 (2021) 1432–1447.
[14] J. Liu, B. Mao, Y. Feng, B. Li, J. Liu, Y. Liu, Closed-loop geometric multi-scale heart-coronary artery model for the numerical calculation of fractional flow reserve, Comput. Methods Programs Biomed. 208 (2021) 106266.
[15] A. Saglietto, M. Fois, L. Ridolfi, G.M. De Ferrari, M. Anselmino, S. Scarsoglio, A computational analysis of atrial fibrillation effects on coronary perfusion across the different myocardial layers, Sci. Rep. 12 (1) (2022) 841.
[16] L. Fan, Y. Sun, J.S. Choy, G.S. Kassab, L.C. Lee, Mechanism of exercise intolerance in heart diseases predicted by a computer model of myocardial demand-supply feedback system, Comput. Methods Programs Biomed. 227 (2022) 107188.
[17] M.S. Olufsen, Structured tree outflow condition for blood flow in larger systemic arteries, Am. J. Physiol., Heart Circ. Physiol. 276 (1) (1999) H257–H268.
[18] N. Westerhof, J.-W. Lankhaar, B.E. Westerhof, The arterial windkessel, Med. Biol. Eng. Comput. 47 (2) (2009) 131–141.
[19] M. Fois, S.V. Maule, M. Giudici, M. Valente, L. Ridolfi, S. Scarsoglio, Cardiovascular response to posture changes: multiscale modeling and in vivo validation during head-up tilt, Front. Physiol. 13 (2022) 123.
[20] M.U. Qureshi, N.A. Hill, A computational study of pressure wave reflections in the pulmonary arteries, J. Math. Biol. 71 (6) (2015) 1525–1549.
[21] Z. Duanmu, W. Chen, H. Gao, X. Yang, X. Luo, N.A. Hill, A one-dimensional hemodynamic model of the coronary arterial tree, Front. Physiol. 10 (2019) 853.
[22] G.D. Vaughan, Pulse propagation in the pulmonary and systemic arteries, Ph.D. thesis, University of Glasgow, 2010.
[23] M.U. Qureshi, Simulating the pulse wave in the human pulmonary circulation, Ph.D. thesis, University of Glasgow, 2013.
[24] D.E. Gregg, H.D. Green, Registration and interpretation of normal phasic inflow into a left coronary artery by an improved differential manometric method, Am. J. Physiol., Legacy Content 130 (1) (1940) 114–125.
[25] A.G. Goodwill, G.M. Dick, A.M. Kiel, J.D. Tune, Regulation of coronary blood flow, Compr. Physiol. 7 (2) (2017) 321.
[26] J.M. Downey, E.S. Kirk, Distribution of the coronary blood flow across the canine heart wall during systole, Circ. Res. 34 (2) (1974) 251–257.
[27] D. Nematzadeh, J. Rose, T. Schryver, H. Huang, P. Kot, Analysis of methodology for measurement of intramyocardial pressure, Basic Res. Cardiol. 79 (1) (1984) 86–97.
[28] D. Algranati, G.S. Kassab, Y. Lanir, Mechanisms of myocardium-coronary vessel interaction, Am. J. Physiol., Heart Circ. Physiol. 298 (3) (2010) H861–H873.
[29] N. Smith, C. Stevens, P. Hunter, Computational modeling of ventricular mechanics and energetics, Appl. Mech. Rev. 58 (2) (2005) 77–90.
[30] L. Fan, R. Namani, J.S. Choy, G.S. Kassab, L.C. Lee, Effects of mechanical dyssynchrony on coronary flow: insights from a computational model of coupled coronary perfusion with systemic circulation, Front. Physiol. 11 (2020) 915.
[31] L. Fan, R. Namani, J.S. Choy, G.S. Kassab, L.C. Lee, Transmural distribution of coronary perfusion and myocardial work density due to alterations in ventricular loading, geometry and contractility, Front. Physiol. (2021) 2105.

[32] G.A. Holzapfel, R.W. Ogden, Constitutive modelling of passive myocardium: a structurally based framework for material characterization, Philos. Trans. R. Soc. A, Math. Phys. Eng. Sci. 367 (1902) (2009) 3445–3475.
[33] H. Gao, H. Wang, C. Berry, X. Luo, B.E. Griffith, Quasi-static image-based immersed boundary-finite element model of left ventricle under diastolic loading, Int. J. Numer. Methods Biomed. Eng. 30 (11) (2014) 1199–1222.
[34] K.L. Sack, E. Aliotta, D.B. Ennis, J.S. Choy, G.S. Kassab, J.M. Guccione, T. Franz, Construction and validation of subject-specific biventricular finite-element models of healthy and failing swine hearts from high-resolution DT-MRI, Front. Physiol. 9 (2018) 539.
[35] A.D. Wisneski, Y. Wang, S. Cutugno, S. Pasta, A. Stroh, J. Yao, T.C. Nguyen, V.S. Mahadevan, J.M. Guccione, Left ventricle biomechanics of low-flow, low-gradient aortic stenosis: a patient-specific computational model, Front. Physiol. (2022) 587.
[36] D. Guan, Y. Wang, L. Xu, L. Cai, X. Luo, H. Gao, Effects of dispersed fibres in myocardial mechanics, part II: active response, Math. Biosci. Eng. 19 (4) (2022) 4101–4119.
[37] M.S. Olufsen, Modeling the arterial system with reference to an anestesia simulator, Ph.D. thesis, Roskilde University, 1998.
[38] D.A. Dowe, M. Fioranelli, P. Pavone, Imaging Coronary Arteries, Springer, 2013.
[39] F. Saremi, Muresian, Coronary veins: comprehensive CT-anatomic classification and review of variants and clinical implications, Radiographics 32 (1) (2012) E1–E32.
[40] R. Potter, A. Groom, Capillary diameter and geometry in cardiac and skeletal muscle studied by means of corrosion casts, Microvasc. Res. 25 (1) (1983) 68–84.
[41] M. Ldinghausen, The Venous Drainage of the Human Myocardium, Springer Science and Business Media, 2012.
[42] G.S. Kassab, D.H. Lin, Y. Fung, Morphometry of pig coronary venous system, Am. J. Physiol., Heart Circ. Physiol. 267 (6) (1994) H2100–H2113.
[43] S.S. Shah, S.D. Teague, J.C. Lu, A.L. Dorfman, E.A. Kazerooni, P.P. Agarwal, Imaging of the coronary sinus: normal anatomy and congenital abnormalities, Radiographics 32 (4) (2012) 991–1008.
[44] R. Mlynarski, A. Mlynarska, M. Haberka, K.S. Golba, M. Sosnowski, The thebesian valve and coronary sinus in cardiac magnetic resonance, J. Interv. Cardiac Electrophysiol. 43 (2) (2015) 197–203.
[45] L. Mehra, S. Raheja, S. Agarwal, Y. Rani, K. Kaur, A. Tuli, Anatomical consideration and potential complications of coronary sinus catheterisation, J. Clin. Diagn. Res. 10 (2) (2016) AC12.
[46] G. Kassab, S. Molloi, Cross-sectional area and volume compliance of porcine left coronary arteries, Am. J. Physiol., Heart Circ. Physiol. 281 (2) (2001) H623–H628.
[47] M. Poloni, D. Winterbone, J. Nichols, Comparison of unsteady flow calculations in a pipe by the method of characteristics and the two-step differential Lax-Wendroff method, Int. J. Mech. Sci. 29 (5) (1987) 367–378.
[48] H. Gao, A. Aderhold, K. Mangion, X. Luo, D. Husmeier, C. Berry, Changes and classification in myocardial contractile function in the left ventricle following acute myocardial infarction, J. R. Soc. Interface 14 (132) (2017) 20170203.
[49] J.D. Bayer, R.C. Blake, G. Plank, N.A. Trayanova, A novel rule-based algorithm for assigning myocardial fiber orientation to computational heart models, Ann. Biomed. Eng. 40 (10) (2012) 2243–2254.
[50] J. Wong, E. Kuhl, Generating fibre orientation maps in human heart models using Poisson interpolation, Comput. Methods Biomech. Biomed. Eng. 17 (11) (2014) 1217–1226.
[51] H. Wang, H. Gao, X. Luo, C. Berry, B. Griffith, R. Ogden, T. Wang, Structure-based finite strain modelling of the human left ventricle in diastole, Int. J. Numer. Methods Biomed. Eng. 29 (1) (2013) 83–103.
[52] B. Baillargeon, N. Rebelo, D.D. Fox, R.L. Taylor, E. Kuhl, The living heart project: a robust and integrative simulator for human heart function, Eur. J. Mech. A, Solids 48 (2014) 38–47.
[53] J. Guccione, A. McCulloch, Mechanics of active contraction in cardiac muscle: part I—constitutive relations for fiber stress that describe deactivation, J. Biomech. Eng. 115 (1) (1993) 72–81.
[54] N. Thekkethil, S. Rossi, H. Gao, S.I.H. Richardson, B.E. Griffith, X. Luo, A stabilized linear finite element method for anisotropic poroelastodynamics with application to cardiac perfusion, Comput. Methods Appl. Mech. Eng. 405 (2023) 115877.
[55] B.E. Griffith, N.A. Patankar, Immersed methods for fluid–structure interaction, Annu. Rev. Fluid Mech. 52 (2020) 421–448.
[56] T.R. Porter, S.K. Shillcutt, M.S. Adams, G. Desjardins, K.E. Glas, J.J. Olson, R.W. Troughton, Guidelines for the use of echocardiography as a monitor for therapeutic intervention in adults: a report from the American society of echocardiography, J. Am. Soc. Echocardiogr. 28 (1) (2015) 40–56.
[57] M.D. Cerqueira, N.J. Weissman, V. Dilsizian, A.K. Jacobs, S. Kaul, W.K. Laskey, D.J. Pennell, J.A. Rumberger, T. Ryan, et al., Standardized myocardial segmentation and nomenclature for tomographic imaging of the heart: a statement for healthcare professionals from the cardiac imaging committee of the council on clinical cardiology of the American heart association, Circulation 105 (4) (2002) 539–542.
[58] R.J. Cerci, A. Arbab-Zadeh, R.T. George, J.M. Miller, A.L. Vavere, V. Mehra, K. Yoneyama, J. Texter, C. Foster, W. Guo, et al., Aligning coronary anatomy and myocardial perfusion territories: an algorithm for the CORE320 multicenter study, Circ. Cardiovasc. Imag. 5 (5) (2012) 587–595.
[59] S. Dassault, Abaqus Analysis User's Guide (6.13), Simulia Corp, Providence, Rhode Island, United States, 2014.
[60] R. Erbel, F. Alfonso, C. Boileau, O. Dirsch, B. Eber, A. Haverich, H. Rakowski, J. Struyven, K. Radegran, U. Sechtem, et al., Diagnosis and management of aortic dissection: task force on aortic dissection, European society of cardiology, Eur. Heart J. 22 (18) (2001) 1642–1681.
[61] P. Reymond, N. Westerhof, N. Stergiopulos, Systolic hypertension mechanisms: effect of global and local proximal aorta stiffening on pulse pressure, Ann. Biomed. Eng. 40 (3) (2012) 742–749.
[62] R.A. Nishimura, C.M. Otto, R.O. Bonow, B.A. Carabello, J.P. Erwin III, L.A. Fleisher, H. Jneid, M.J. Mack, C.J. McLeod, P.T. O'Gara, et al., 2017 AHA/ACC focused update of the 2014 AHA/ACC guideline for the management of patients with valvular heart disease: a report of the American college of cardiology/American heart association task force on clinical practice guidelines, Circulation 135 (25) (2017) e1159–e1195.
[63] G. Mahadevan, R. Davis, M. Frenneaux, F. Hobbs, G. Lip, J. Sanderson, M. Davies, Left ventricular ejection fraction: are the revised cut-off points for defining systolic dysfunction sufficiently evidence based?, Heart 94 (4) (2008) 426–428.
[64] R.M. Lang, L.P. Badano, V. Mor-Avi, J. Afilalo, A. Armstrong, L. Ernande, F.A. Flachskampf, E. Foster, S.A. Goldstein, T. Kuznetsova, et al., Recommendations for cardiac chamber quantification by echocardiography in adults: an update from the American society of echocardiography and the European association of cardiovascular imaging, Eur. Heart J., Cardiovasc. Imag. 16 (3) (2015) 233–271.
[65] M. Genet, L.C. Lee, R. Nguyen, H. Haraldsson, G. Acevedo-Bolton, Z. Zhang, L. Ge, K. Ordovas, S. Kozerke, J.M. Guccione, Distribution of normal human left ventricular myofiber stress at end diastole and end systole: a target for in silico design of heart failure treatments, J. Appl. Physiol. 117 (2) (2014) 142–152.
[66] A.D. Wisneski, Y. Wang, T. Deuse, A.C. Hill, S. Pasta, K.L. Sack, J. Yao, J.M. Guccione, Impact of aortic stenosis on myofiber stress: translational application of left ventricle-aortic coupling simulation, Front. Physiol. (2020) 1157.
[67] K.L. Sack, B. Baillargeon, G. Acevedo-Bolton, M. Genet, N. Rebelo, E. Kuhl, L. Klein, G.M. Weiselthaler, D. Burkhoff, T. Franz, et al., Partial lvad restores ventricular outputs and normalizes lv but not rv stress distributions in the acutely failing heart in silico, Int. J. Artif. Organs 39 (8) (2016) 421–430.
[68] Y. Fan, W. Ronan, I. Teh, J.E. Schneider, C.E. Varela, W. Whyte, P. McHugh, S. Leen, E. Roche, A comparison of two quasi-static computational models for assessment of intra-myocardial injection as a therapeutic strategy for heart failure, Int. J. Numer. Methods Biomed. Eng. 35 (9) (2019) e3213.
[69] J.P. Mynard, D.J. Penny, J.J. Smolich, Scalability and in vivo validation of a multiscale numerical model of the left coronary circulation, Am. J. Physiol., Heart Circ. Physiol. 306 (4) (2014) H517–H528.
[70] K.D. Knott, C. Camaioni, A. Ramasamy, J.A. Augusto, A.N. Bhuva, H. Xue, C. Manisty, R.K. Hughes, L.A. Brown, R. Amersey, et al., Quantitative myocardial perfusion in coronary artery disease: a perfusion mapping study, J. Magn. Reson. Imaging 50 (3) (2019) 756–762.
[71] M. Zamir, H. Chee, Branching characteristics of human coronary arteries, Can. J. Physiol. Pharm. 64 (6) (1986) 661–668.
[72] G.S. Kassab, C.A. Rider, N.J. Tang, Y.-C. Fung, Morphometry of pig coronary arterial trees, Am. J. Physiol., Heart Circ. Physiol. 265 (1) (1993) H350–H365.
[73] A. Zoumi, X. Lu, G.S. Kassab, B.J. Tromberg, Imaging coronary artery microstructure using second-harmonic and two-photon fluorescence microscopy, Biophys. J. 87 (4) (2004) 2778–2786.
[74] N.P. Smith, A. Pullan, P. Hunter, Generation of an anatomically based geometric coronary model, Ann. Biomed. Eng. 28 (1) (2000) 14–25.
[75] B. Kaimovitz, Y. Lanir, G.S. Kassab, Large-scale 3-d geometric reconstruction of the porcine coronary arterial vasculature based on detailed anatomical data, Ann. Biomed. Eng. 33 (11) (2005) 1517–1535.
[76] B. Kaimovitz, Y. Lanir, G.S. Kassab, A full 3-d reconstruction of the entire porcine coronary vasculature, Am. J. Physiol., Heart Circ. Physiol. 299 (4) (2010) H1064–H1076.
[77] A. Goyal, J. Lee, P. Lamata, J. van den Wijngaard, P. van Horssen, J. Spaan, M. Siebes, V. Grau, N.P. Smith, Model-based vasculature extraction from optical fluorescence cryomicrotome images, IEEE Trans. Med. Imaging 32 (1) (2012) 56–72.
[78] Y.A. Chen, E.T. Nguyen, C. Dennie, R.M. Wald, A.M. Crean, S.-J. Yoo, L. Jimenez-Juan, Computed tomography and magnetic resonance imaging of the coronary sinus: anatomic variants and congenital anomalies, Insights Imaging 5 (5) (2014) 547–557.
[79] L.A. Brown, S.C. Onciul, D.A. Broadbent, K. Johnson, G.J. Fent, J.R. Foley, P. Garg, P.G. Chew, K. Knott, E. Dall'Armellina, et al., Fully automated, inline quantification of myocardial blood flow with cardiovascular magnetic resonance: repeatability of measurements in healthy subjects, J. Cardiovasc. Magn. Reson. 20 (1) (2018) 1–12.
[80] T. Kotecha, A. Martinez-Naharro, M. Boldrini, D. Knight, P. Hawkins, S. Kalra, D. Patel, G. Coghlan, J. Moon, S. Plein, et al., Automated pixel-wise quantitative myocardial perfusion mapping by CMR to detect obstructive coronary artery disease and coronary microvascular dysfunction: validation against invasive coronary physiology, JACC Cardiovasc. Imag. 12 (10) (2019) 1958–1969.
[81] C.J. Salton, M.L. Chuang, C.J. O'Donnell, M.J. Kupka, M.G. Larson, K.V. Kissinger, R.R. Edelman, D. Levy, W.J. Manning, Gender differences and normal left ventricular anatomy in an adult population free of hypertension: a cardiovascular magnetic resonance study of the framingham heart study offspring cohort, J. Am. Coll. Cardiol. 39 (6) (2002) 1055–1060.
[82] C.G. Caro, T.J. Pedley, R. Schroter, W. Seed, The Mechanics of the Circulation, Cambridge University Press, 2012.
[83] H. Kanatsuka, N. Sekiguchi, K. Sato, K. Akai, Y. Wang, T. Komaru, K. Ashikawa, T. Takishima, Microvascular sites and mechanisms responsible for reactive hyperemia

in the coronary circulation of the beating canine heart, Circ. Res. 71 (4) (1992) 912–922.
[84] S. Scarsoglio, C. Gallo, A. Saglietto, L. Ridolfi, M. Anselmino, Impaired coronary blood flow at higher heart rates during atrial fibrillation: investigation via multiscale modelling, Comput. Methods Programs Biomed. 175 (2019) 95–102.
[85] C. Gallo, L. Ridolfi, S. Scarsoglio, Cardiovascular deconditioning during long-term spaceflight through multiscale modeling, npj Microgravity 6 (1) (2020) 27.
[86] J. Liu, B. Li, Y. Zhang, L. Zhang, S. Huang, H. Sun, J. Liu, X. Zhao, M. Zhang, W. Wang, et al., A high-fidelity geometric multiscale hemodynamic model for predicting myocardial ischemia, Comput. Methods Programs Biomed. 233 (2023) 107476.
[87] S. Claridge, N. Briceno, Z. Chen, K. De Silva, B. Modi, T. Jackson, J.M. Behar, S. Niederer, C.A. Rinaldi, D. Perera, Changes in contractility determine coronary haemodynamics in dyssynchronous left ventricular heart failure, not vice versa, IJC Heart Vasc. 19 (2018) 8–13.
[88] G. Heusch, Myocardial ischemia: lack of coronary blood flow, myocardial oxygen supply-demand imbalance, or what?, Am. J. Physiol., Heart Circ. Physiol. 316 (6) (2019) H1439–H1446.